STS-1 Forward RCS Oxidizer Tank Subsystem Failure Assessment

Conference Paper · January 2021

DOI: 10.2514/6.2021-1617

2 authors:

K. Chauncey Wu
NASA
67 PUBLICATIONS **999** CITATIONS
SEE PROFILE

John Zipay
NASA
10 PUBLICATIONS **14** CITATIONS
SEE PROFILE

AIAA 2021-1617

STS-1 Forward RCS Oxidizer Tank Subsystem Failure Assessment

K. Chauncey Wu
NASA Langley Research Center
Hampton, Virginia

John J. Zipay
NASA Johnson Space Center
Houston, Texas

2021 AIAA Science and Technology Forum and Exposition
11-15 & 19-21 January 2021

STS-1 Forward RCS Oxidizer Tank Subsystem Failure Assessment

K. Chauncey Wu[1]
NASA Langley Research Center
Hampton, Virginia

John J. Zipay[2]
NASA Johnson Space Center
Houston, Texas

Abstract

The launch of the Space Shuttle* Columbia *on STS-1 marked the beginning of a new era in American spaceflight. It was the only crewed first flight of a launch vehicle to date, and was also the first crewed system to use large solid rockets as primary propulsion. A potential disaster was narrowly averted at liftoff when an ignition overpressure pulse swept up the Shuttle stack. The frequency of this transient shock wave exceeded pre-launch predictions, and resulted in high, alternating normal accelerations along the length of the vehicle. Among the results of this unexpected loading was failure of an oxidizer tank support strut in the orbiter's forward reaction control system module, which could have led to loss of the mission, crew, and vehicle. This particular incident is investigated in more detail using classical structural mechanics, and the results are discussed to provide additional insight.

I. Introduction

The April 1981 launch of STS-1 (Fig. 1), the first flight of the Space Shuttle *Columbia*, was and remains a major milestone in the history of American spaceflight (Refs. 1, 2). Until its retirement in 2011, the Space Transportation System (STS) or Space Shuttle was the United States' sole capability for launching astronauts, and was the first launch vehicle to feature major component reusability (Refs. 2, 3). Over 135 flights and the next 30 years, *Columbia* and her sister orbiters were used to launch, assemble and service the International Space Station, launch and service the Hubble Space Telescope and other spacecraft for NASA, commercial, and military customers, and perform research in space physics, life sciences, and many other topics.

The losses of the orbiters *Challenger* (STS-51-L, 1986) and *Columbia* (STS-107, 2003) and their crews were tragic milestones in the long history of the Space Shuttle program. However, the failure of a forward reaction control system (RCS) oxidizer tank support strut on STS-1 could have led to loss of that crew, vehicle, and mission much earlier, on the program's first flight. That particular incident is investigated here in more detail using classical structural mechanics, with discussion of the results to provide additional insight.

II. Space Shuttle

The orbiter *Columbia*, with a liftoff mass of 208,440 lbm and a 10,820 lbm payload, was launched into a 40.3-degree inclination, 148-nautical mile circular low Earth orbit in the early morning of April 12, 1981 (Refs. 3, 4). At liftoff (Fig. 1), the winged orbiter was attached to

---

[1] Acquisition Manager, Science Office for Mission Assessments. AIAA Associate Fellow.
[2] Deputy Chief, Structures Branch, Engineering Directorate. AIAA Associate Fellow.

Figure 1. Space Shuttle *Columbia* launch (STS-1)

the expendable external tank (ET) and two solid rocket boosters (SRBs), with a system launch mass of approximately 4.46 million lbm.

The orbiter (Fig. 2) was 122 ft overall length with a 78-ft wingspan. The tip of its vertical tail was 57 ft above ground level when sitting on its deployed landing gear. Major orbiter components included a pressurized, three-level (flight deck, mid-deck, and lower equipment bay) crew module with airlock, a 60 ft-long, 15 ft-diameter cylindrical payload bay, three main engines (SSMEs), avionics, electrical power system, orbital maneuvering system (OMS), RCS, and a thermal protection system. Double-delta wings, wheeled landing gear, and aerodynamic control surfaces were used for unpowered atmospheric flight to a runway landing.

The 154 ft-long, 28 ft-diameter ET contained the 1.59 million lbm of liquid oxygen and liquid hydrogen propellants fed to the three SSMEs installed in the orbiter's aft fuselage, and had a dry mass of 77,500 lbm. Each of the two 149 ft-long, 12 ft-diameter cylindrical SRBs provided 3.3 million lbf of thrust on liftoff, contained 1.1 million lbm of solid propellant, and had a dry mass of 193,000 lbm. Before launch, the fully fueled Shuttle stack was cantilevered from eight discrete attachment points on a mobile launch platform (MLP). Three large cutouts in the MLP allowed exhaust from the SSMEs and SRBs to be directed away from the vehicle through a blast deflector and flame trench.

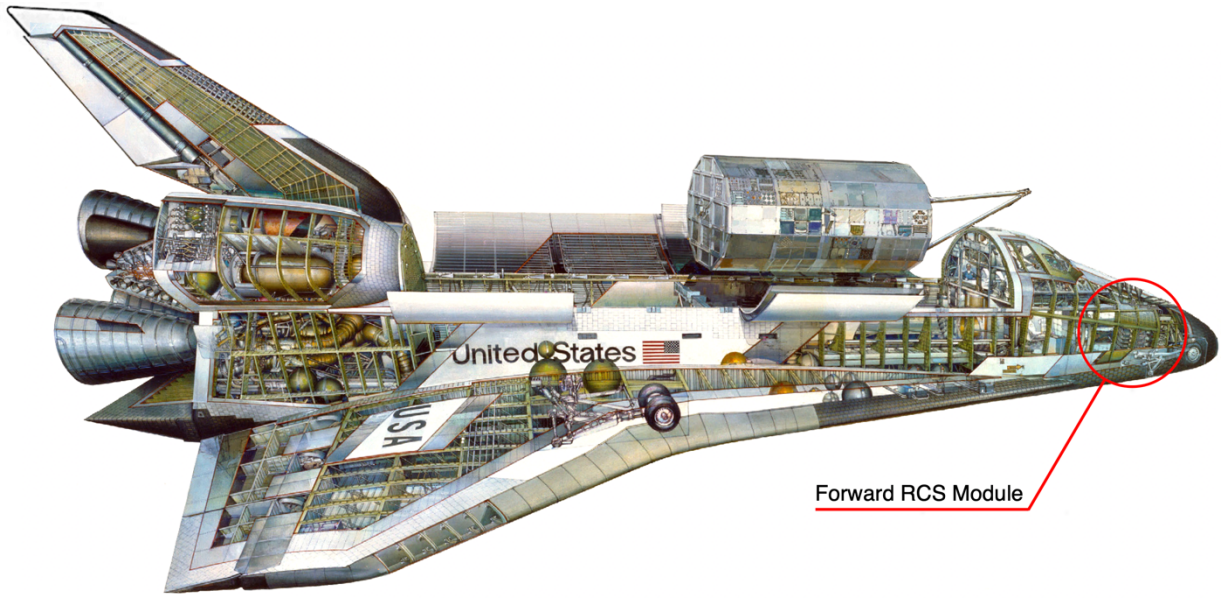

Figure 2. Space Shuttle orbiter

III. STS-1 Launch

The STS-1 mission was the only crewed first flight of an American launch vehicle, and was the first system to feature reusability of many of its major components. The Shuttle was also the first human-rated system to use large solid rockets as primary propulsion, with the liquid-propellant SSMEs contributing only about 15 percent of the liftoff thrust. A potential disaster was avoided at liftoff when the SRBs' ignition overpressure pulse (Refs. 5, 6, 7, 8) swept upwards along the Shuttle stack. While the amplitude of the actual environment was within 5 percent of the pre-launch predictions, the natural frequency of this transient shock wave was significantly greater than the predicted behavior. The frequency of the pulse was also close to the system's natural frequency, and resulted in an orbiter dynamic response that far exceeded predictions from pre-launch analyses.

The Shuttle system's response to the SRB ignition overpressure resulted in high, alternating Z axis (normal) loading along the vehicle's length that excited the first bending mode of the orbiter fuselage. Among the results of this unexpected loading (Fig. 3, from Ref. 4) was a structural failure of an oxidizer tank aft support strut in the orbiter's forward RCS module. More extensive structural failures could have resulted in oxidizer leaks within that compartment, and possible explosive reaction with the volatile RCS fuel or other chemicals. The potential consequences of this incident, and others detailed in Ref. 4, could have led to the loss of the mission, crew and vehicle.

IV. Orbiter Reaction Control System

The orbiter's RCS thrusters used a combination of nitrogen tetroxide (N_2O_4) oxidizer and monomethyl hydrazine (MMH) fuel to effect vehicle attitude and translational control in orbit, and during reentry outside the atmosphere and to Mach 1 (Refs. 9, 10). These hypergolic propellants (260 seconds specific impulse) were fed to the thrusters using gaseous helium (He) pressurant stored at 3,600 lbf/in^2 and regulated to 245 lbf/in^2, where the propellants were combined in a 1.6:1 oxidizer-fuel mass ratio to produce the desired thrust.

A total of 38 primary thrusters (870 lbf thrust each) and six vernier thrusters (24 lbf thrust each) were deployed in three separate modules installed around the orbiter. The forward RCS

(FRCS) module (Figs. 2 and 4) was located in the orbiter's forward fuselage above the nose landing gear and ahead of the crew module, and contained 14 primary thrusters and two vernier thrusters grouped and oriented along the vehicle's principal axes. The FRCS module had a dry mass of 2,680 lbm and a conventional aluminum semi-monocoque primary structure. As shown in Fig. 4 (Ref. 11), a spherical oxidizer tank was located on the +Y side (right, facing forward) of the FRCS module, and an identical fuel tank was mounted on the −Y side (left, facing forward). Both tanks had an 18.0 ft^3 internal volume and a 350 lbf/in^2 maximum operating pressure.

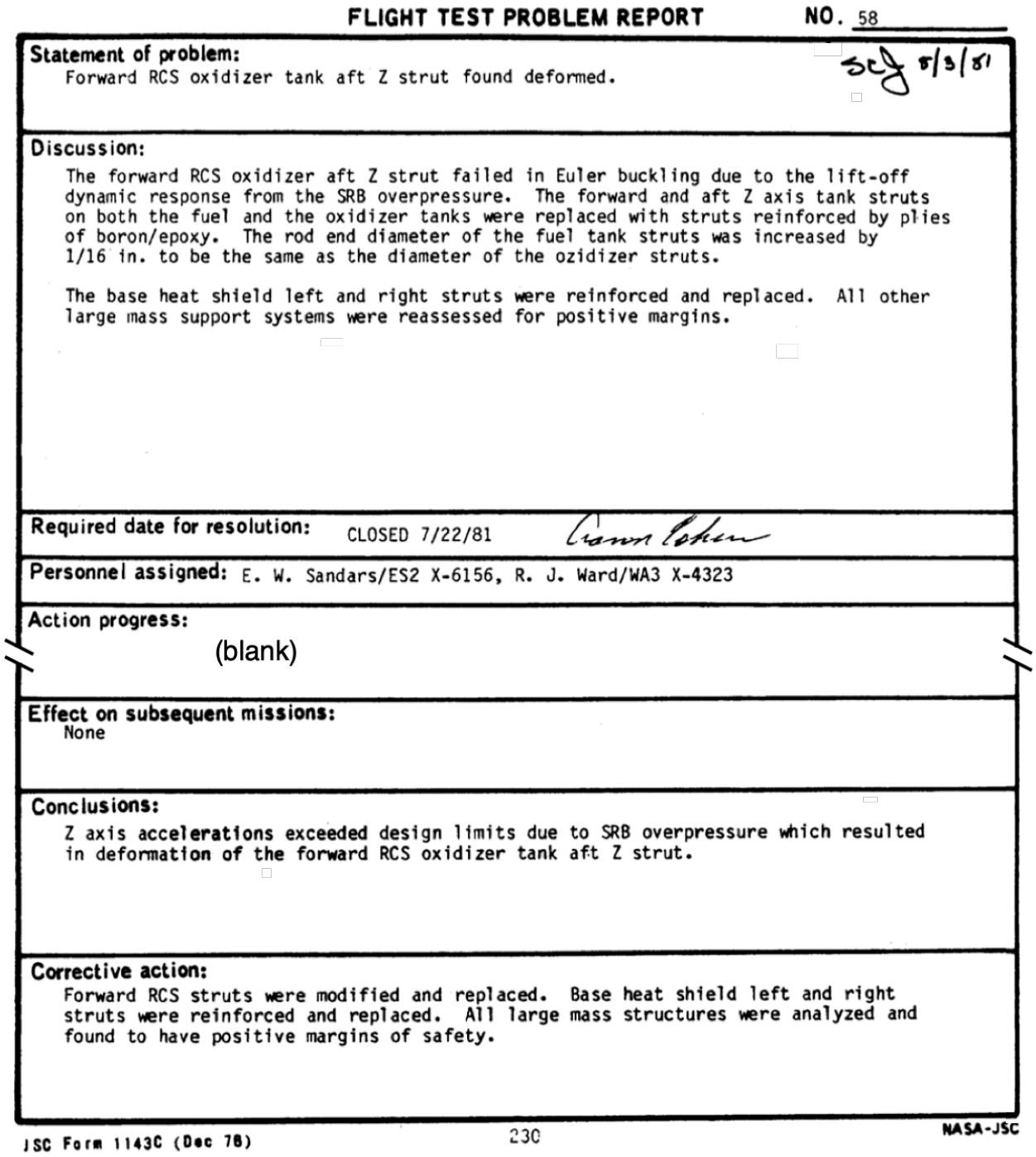

FLIGHT TEST PROBLEM REPORT NO. 58

Statement of problem:
Forward RCS oxidizer tank aft Z strut found deformed.

SCJ 8/3/81

Discussion:
The forward RCS oxidizer aft Z strut failed in Euler buckling due to the lift-off dynamic response from the SRB overpressure. The forward and aft Z axis tank struts on both the fuel and the oxidizer tanks were replaced with struts reinforced by plies of boron/epoxy. The rod end diameter of the fuel tank struts was increased by 1/16 in. to be the same as the diameter of the ozidizer struts.

The base heat shield left and right struts were reinforced and replaced. All other large mass support systems were reassessed for positive margins.

Required date for resolution: CLOSED 7/22/81

Personnel assigned: E. W. Sandars/ES2 X-6156, R. J. Ward/WA3 X-4323

Action progress:
(blank)

Effect on subsequent missions:
None

Conclusions:
Z axis accelerations exceeded design limits due to SRB overpressure which resulted in deformation of the forward RCS oxidizer tank aft Z strut.

Corrective action:
Forward RCS struts were modified and replaced. Base heat shield left and right struts were reinforced and replaced. All large mass structures were analyzed and found to have positive margins of safety.

JSC Form 1143C (Dec 78) 230 NASA-JSC

Figure 3. In-Flight Anomaly Report STS-1-V-58 (Ref. 4)

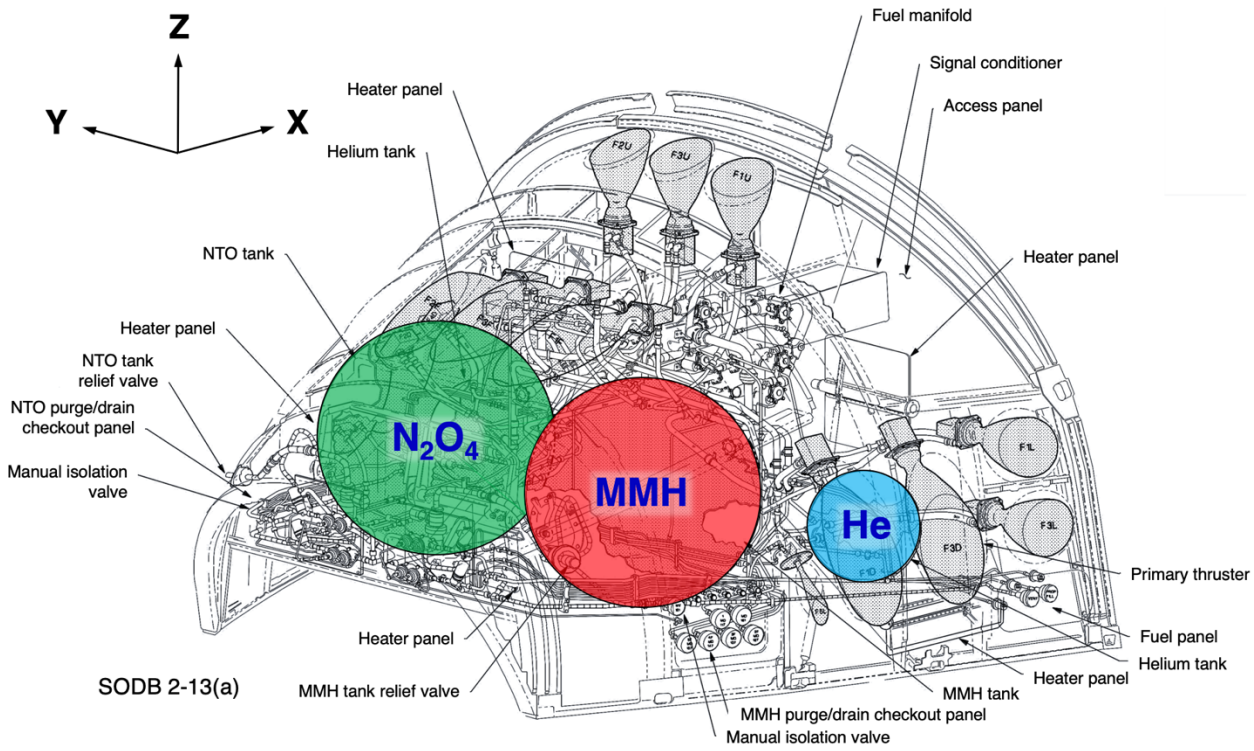

Figure 4. Forward RCS module and components

Each of the two aft RCS modules contained 12 primary thrusters and two vernier thrusters. The OMS engines (6,000 lbf thrust, 315 seconds specific impulse) and their larger propellant tankage were co-located with the aft RCS modules on both sides of the base of the vertical tail behind the payload bay. The common propellants could also be cross-fed between the OMS and aft RCS systems, allowing greater operational flexibility.

In addition to the propellant tanks and thrusters, each RCS module also contained two 17.9-in. inner diameter, Kevlar® 49/epoxy composite-overwrapped pressure vessels (COPVs), indicated in Fig. 4, for helium gas storage, heaters and insulation for thermal control, and redundant manifolds, valves, regulators, and lines for propellant and pressurant distribution.

V. RCS Propellant Tank and Support Structure

Each RCS module contained two thin-walled, titanium-alloy (Ti-6Al-4V) tanks (Refs. 12, 13) for propellant storage. Each propellant tank had a nominal inner diameter of 39.0 in. and a 0.035-in. shell wall thickness. Stainless steel mesh devices were developed to effect propellant acquisition and pressurant separation using surface tension without an internal liner. The tank shells were manufactured in separate hemispheres, and joined with an equatorial weld after integration of the internal surface tension devices. Forward and aft fittings were also installed on each tank for attachment of feedlines and support struts. Each FRCS propellant tank had an empty mass of 72.7 lbm. Each aft RCS propellant tank was slightly heavier at 77.0 lbm.

The FRCS oxidizer tank subsystem is shown in Fig. 5 (Ref. 11). Six tubular struts, designated as Struts *A* through *F*, connected the oxidizer tank to the FRCS module primary structure. These struts were arranged to prevent tank rigid-body spatial motion, and to react applied loads with minimal induced forces and moments on the tank. Revolute joints at both ends of each strut were attached to clevis fittings on the tank and FRCS module airframe to provide moment-less connections. The FRCS fuel tank was supported with an identical strut

arrangement reflected about the X-Z plane, and similar sets of struts were also used to support the smaller pressurant COPVs.

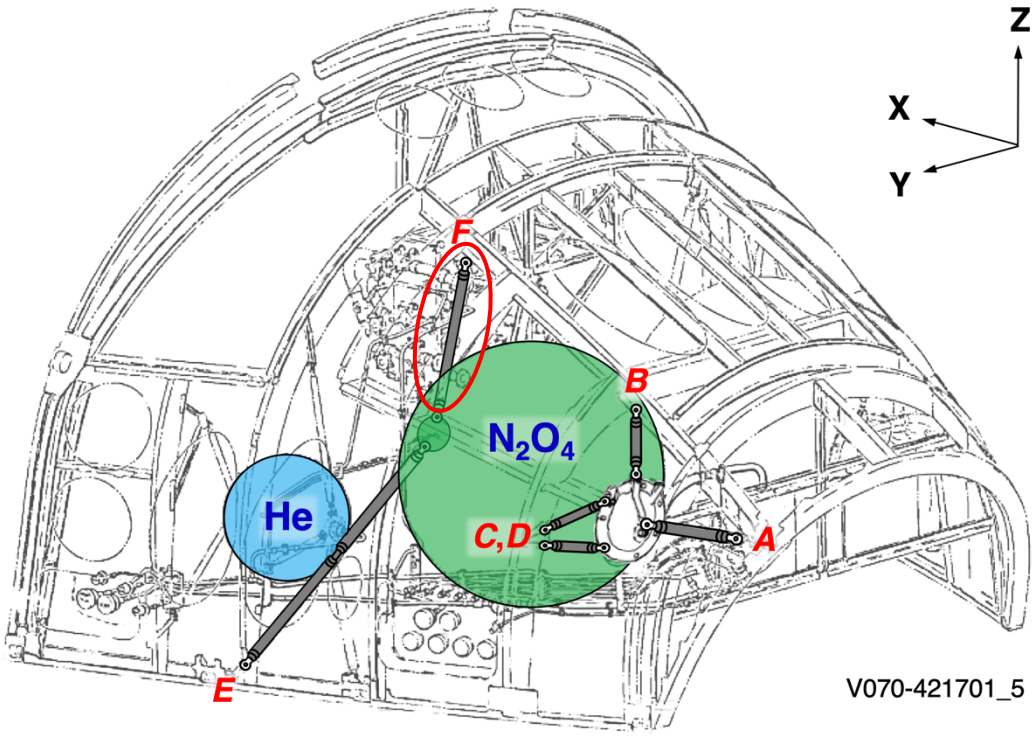

Figure 5. Oxidizer tank subsystem

VI. Tank Support Struts

Four Struts *A* through *D* were attached to the oxidizer tank's forward fitting (Ref. 14), as shown in Fig. 5. From an analysis of their direction cosines, Strut *A* was expected to carry the tank primary launch loads in tension along the orbiter's X (longitudinal) axis, while Strut *B* reacted mostly tank Z (normal) loads. The shortest Struts *C* and *D* reacted mainly tank Y (lateral) loads. Struts *E* and *F* were attached to the tank's aft fitting, with the longest Strut *E* carrying mainly Y loads, and Strut *F* reacting mostly Z loads.

Fig. 3 states that the *"(f)orward RCS oxidizer tank aft Z strut (was) found deformed."* The supporting discussion also states that, "*(t)he … strut failed in Euler buckling …"*. The authors' interpretation of these statements is that Strut *F*, circled in Fig. 5 and also shown in Fig. 6, buckled elastically first, and then experienced local material yielding of the strut wall. Because Euler buckling is a purely elastic failure mode, buckling alone would not show observable damage after the loads were removed. Therefore, the permanent deformation noted must have occurred from plastic material failure due to bending beyond Euler buckling.

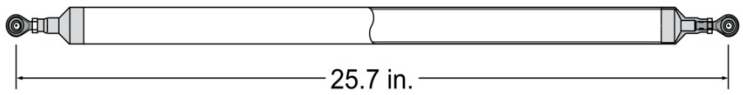

Figure 6. Tank support Strut *F*

Further discussions (Ref. 15) with Mr. Tom Modlin, former Chair of the Shuttle Level II Loads and Dynamics Panel, indicated that the local failure of the strut was marked by a "*slight impression at mid length*", and only noted upon close examination during *Columbia*'s post-flight

inspection and repair. Based on this additional information, the present analyses will therefore assume a minimum failure condition of material yielding at the elastic limit (*i.e.*, onset of plastic behavior) of the struts' midspan cross-section.

Each strut was fabricated from thin-walled, Ti-3Al-2.5V tubing, with machined Ti-6Al-4V end fittings (shown in lighter gray) butt-welded to the tube ends. These end fittings were internally threaded for attachment of Inconel 718 rod-ends (shown in darker gray) with integral spherical bearings to provide pinned-end boundary conditions for the struts. While most of the struts had simple, prismatic central tubes, Strut *E* (Fig. 7) had a solid 3 in.-long, 1 in.-diameter Ti-6Al-4V rod that was welded between two long tubes. This more complex geometry was required to ensure adequate dynamic clearances between the strut's midspan and the adjacent pressurant COPV (Fig. 5). Figs. 6 and 7 are drawn to the same scale.

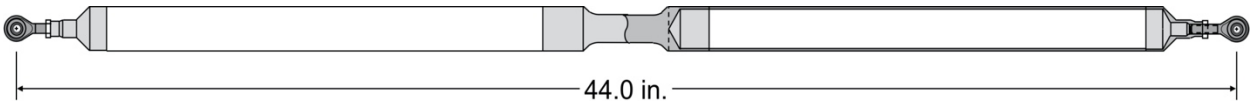

Figure 7. Tank support Strut *E*

The pin-to-pin length L, tube outer radius R, and nominal wall thickness T for Struts *A* through *F* (Ref. 14) are listed in Table 1, along with calculated central tube cross-sectional areas A and moments of inertia I. The diameter and thickness reported for Strut *E* are for the longer tubes, and do not include the solid element shown in Fig. 7. The strut slenderness ratio L/ρ (strut length L divided by the cross-section radius of gyration ρ) ranges from 31.4 for Strut *B* to 86.0 for Strut *E*.

Table 1. Tank support strut dimensions

Strut	L, in.	R, in.	T, in.	A, in^2	I, in^4
A	20.80	0.750	0.054	0.245	0.064
B	9.25	0.438	0.045	0.117	0.010
C, D	12.12	0.438	0.020	0.054	0.005
E	44.00	0.750	0.054	0.245	0.064
F	25.70	0.625	0.026	0.100	0.019

VII. Propellant Tank Masses and Loads

The FRCS module propellant tanks were filled (Ref. 4) with a total load of 1,464 lbm of oxidizer and 923 lbm of fuel (Ref. 16) at launch. After including the 72.7 lbm tank empty mass, the total filled oxidizer tank mass at liftoff is estimated at m_O = 1,537 lbm. The weights of residual propellants and pressurants in the feedlines are not included. While the support strut failure was only noted on the oxidizer tank, the fuel tank subsystem (estimated at 996 lbm full) will also be examined later in this study.

As described in Fig. 3, "*(t)he … strut failed … due the lift-off dynamic response from the SRB overpressure."* Liftoff Z accelerations measured in the orbiter cockpit (Fig. 8) were reported in Refs. 4 and 5 to have a maximum value of +3.5 *g* and a minimum of −2.0 *g*, with a peak-to-peak acceleration of [+3.5 *g* − (−2.0 *g*)] or +5.5 *g*, and a natural frequency of approximately 9.6 Hz. Multiplication of these measured Z accelerations and the filled oxidizer tank mass gives estimates for the maximum inertial Z loading of 5,378 lbf, a minimum value of −3,073 lbf, and a peak-to-peak loading of 8,451 lbf.

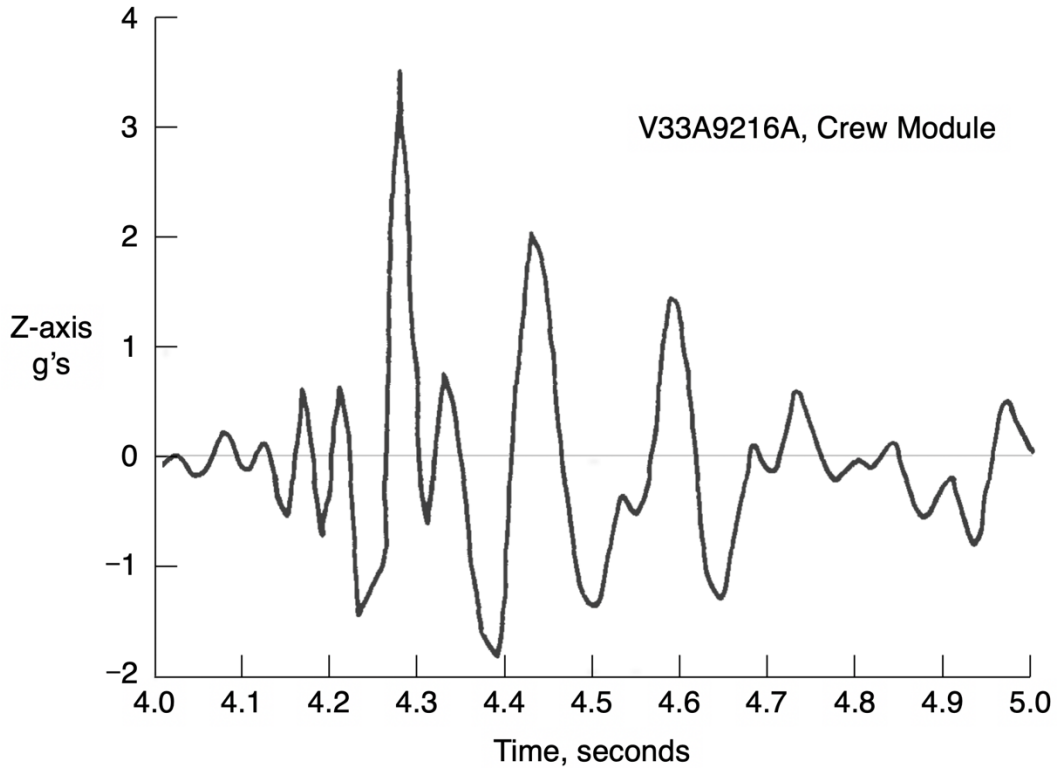

Figure 8. Measured liftoff Z acceleration (Ref. 5)

VIII. Tank Subsystem Structural Analyses

The FRCS oxidizer tank and its support struts are viewed in the −Y direction in Fig. 9. The six pinned-end Struts *A* through *F*, when attached to the FRCS module's structure, form a statically determinate set of constraints to prevent rigid-body motion of the tank (Ref. 17). The axial forces in Struts *A* through *F* can therefore be found from simultaneous solution of the six equilibrium equations,

$$\Sigma F_i = 0;\ i = \mathrm{X, Y, Z} \tag{1a}$$

$$\Sigma M_j = 0;\ j = \mathrm{X, Y, Z.} \tag{1b}$$

A simplified structural model of the oxidizer tank subsystem is shown in Fig. 10. The propellant tank and its contents are replaced by a rigid, massless beam (shown in green) with a point mass *m* at its midspan and zero moments of inertia. The tank symmetry axis in this model, indicated by the dashed line in Fig. 9, is rotated by 8 degrees about the +Y axis (Ref. 14) to be parallel to the X axis. Struts *A* and *B* are also rotated slightly to be parallel to the X and Z axes, respectively, and Struts *C* and *D* are rotated to be in the Y-Z plane.

Equations 1a and 1b are solved in Appendix A for the individual strut axial forces P_i under the applied Z force $m a_Z$, which are,

$$P_A = +fx\, m a_Z/(2fz) \tag{2a}$$

$$P_B = -m a_Z/2 \tag{2b}$$

$$P_C = 0 \tag{2c}$$

$$P_D = 0 \tag{2d}$$

$$P_E = 0 \tag{2e}$$

$$P_F = -m\,a_Z/(2fz) \tag{2f}$$

with the subscripts *A* through *F* denoting specific struts. Strut *A* is in tension as indicated by the positive sign, and Struts *B* and *F* are in compression (negative). The direction cosines calculated for Strut *F* in Fig. 10 are *fx* = 0.2331 and *fz* = 0.9724.

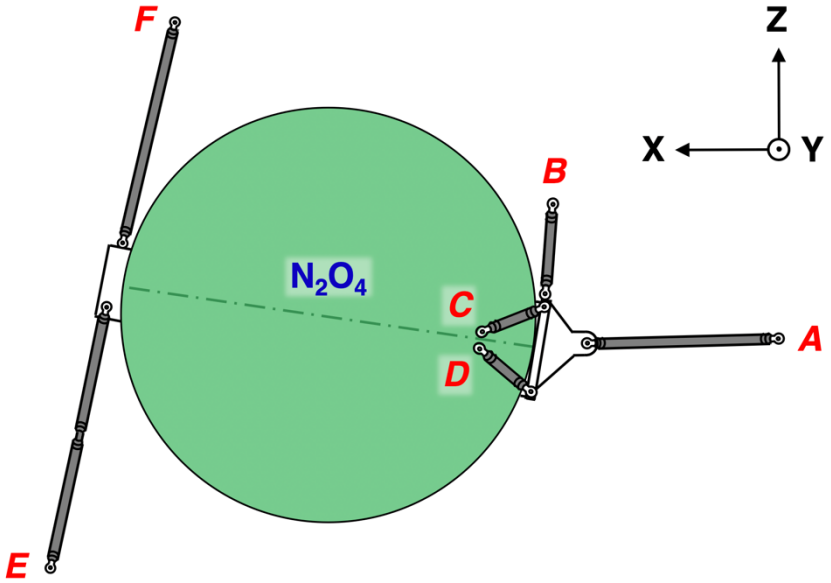

Figure 9. Tank subsystem inboard profile view

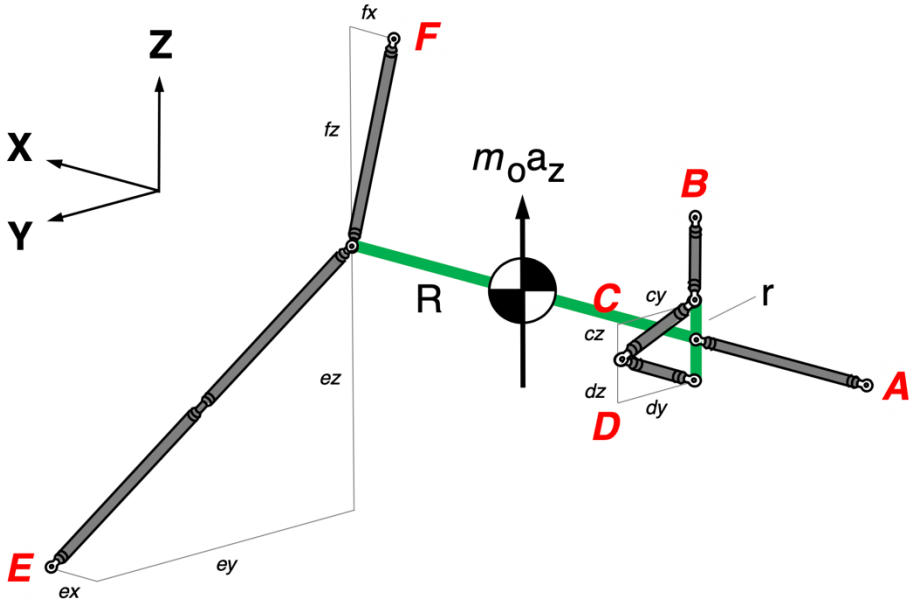

Figure 10. Tank subsystem structural model

IX. Strut Material Properties

Material properties with an A-basis (99 percent probability, 95 percent confidence) allowable level were required during design of this application, as the tank subsystem shown was statically determinate without redundant load paths (Ref. 18). The strut material stress-strain relationships

are also assumed to be identical in tension and compression, linear-elastic with slope E up to the yield stress σ_y, and perfectly plastic with E = 0 thereafter.

Material properties reported in Ref. 14 for the Ti-3Al-2.5V strut tubes are an elastic modulus E = 15.4 Mlbf/in^2, and an A-basis allowable compressive yield stress $\sigma_{cy\text{-}A} = -108$ klbf/in^2. The corresponding mean compressive yield stress $\sigma_{cy\text{-}m} = -125.83$ klbf/in^2 was estimated using the process detailed in Appendix B. The Ti-3Al-2.5V material was received in a cold worked and stress relieved condition, with additional heat treatment before fabrication of the strut tubes.

X. Strut Structural Analyses

Because the axial loads in Struts *C*, *D*, and *E* are zero under the applied loading (Eqns. 2), only Struts *A*, *B*, and *F* are analyzed in this section. A simplified model, shown in Fig. 11, is developed to assess these struts' structural performance. A concentric axial compression load P is applied to a thin-walled tube with pinned-end boundary conditions The uniform central tube is assumed to have a circular cross-section with outer radius R and wall thickness T listed in Table 1. Axial and bending stiffnesses of the end fittings and rod-end bearings on each strut end (see Figs. 7 and 8) are approximated based on their cross-section dimensions. These analyses assume that the struts have no initial geometric imperfections. Any imperfections present in the actual struts could have significantly reduced their buckling loads.

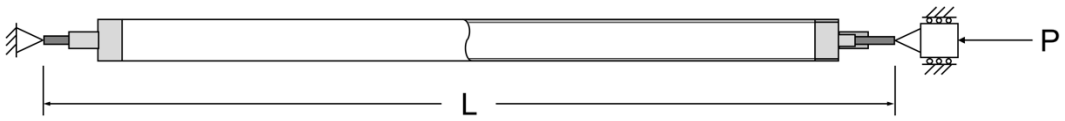

Figure 11. Strut analysis model

The idealized axial load-deformation behavior of this strut is assumed to be linear with slope (*i.e.*, axial stiffness) K_{axial} up to buckling at P_{crit}, as plotted schematically along path 0-1 in Fig. 12a. The axial deformation Δ_{crit} corresponding to buckling is assumed to be the ratio of the buckling load P_{crit} and slope K_{axial}. The buckling load provides an upper limit for the strut axial load. After buckling the axial response is also linear but with zero slope, following path 1-2 as shown in the figure.

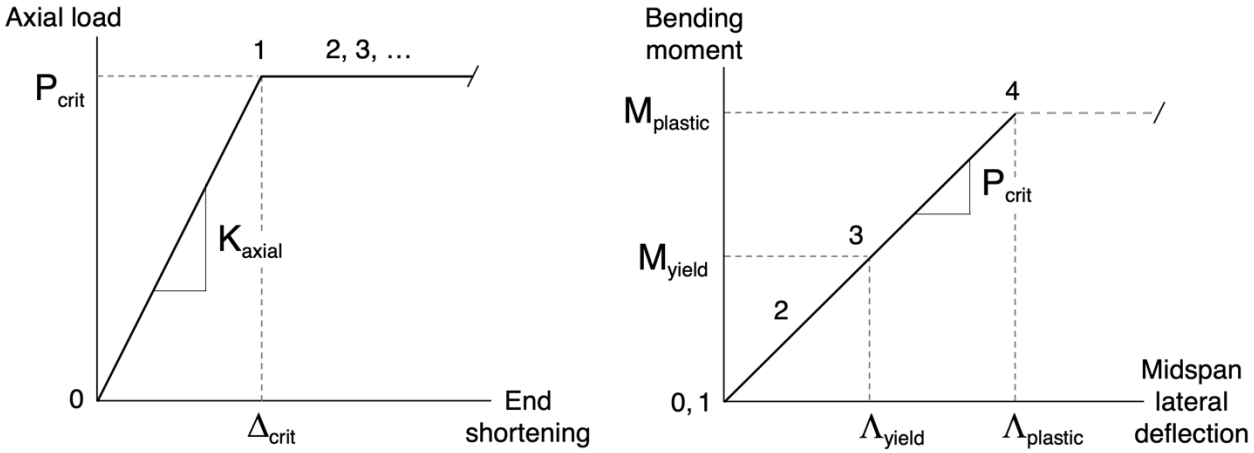

(a) Axial response. (b) Lateral response.

Figure 12. Strut structural response

The idealized strut pre-buckling response of axial compression, no bending, and no lateral deflection (path 0-1) transitions rapidly at buckling (point 1) to post-buckling. This post-buckling response (path 1-2) has nonzero bending under constant axial load P_{crit}, indeterminate axial deformation $\Delta > \Delta_{crit}$, and lateral deflection $\Lambda > 0$. Under a linear combination of the buckling load and increasing bending, the resulting strut response is linear-elastic up to the onset of material yielding at point 3 in Fig. 12b.

The effective axial stiffness K_{axial} for the strut model in Fig. 11 is calculated as,

$$K_{axial} = [\Sigma (l/EA)_i]^{-1}, \quad i = 1, 2, \ldots 6 \tag{3}$$

where the subscript i indicates properties for each separate strut component shown above. For only the central tubes with cross-sectional properties in Table 1, application of this equation with $i = 1$ and $l = L$ gives the baseline tube axial stiffnesses presented in Table 2. After inclusion of the axial stiffnesses of the strut end fittings and rod-end bearings, the resulting strut axial stiffnesses are estimated and reported in Table 3. Buckling loads are not reported in the tables for Strut *A* since its axial load (Eqn. 2a) is tensile under the applied loading.

Table 2. Baseline tube performance

Strut	L/ρ	K_{axial}, lbf/in.	P_{euler}, lbf	P_{johns}, lbf	P_{yield}, lbf
A	40.7	181,622	—	—	***30,867***
B	31.4	195,588	−18,067	−11,757	−14,782
F	59.4	59,909	−4,310	−3,403	−12,580

Table 3. Modified strut performance

Strut	L/ρ	K_{axial}, lbf/in.	P_{euler}, lbf	P_{johns}, lbf	Δ_{crit}, in.
A	40.7	170,788	—	—	0.181
B	31.4	252,260	−16,823	***−10,947***	−0.043
F	59.4	67,555	***−4,242***	−3,349	−0.063

While a strut loaded in compression will typically fail in buckling, the specific failure mode that the strut will experience is a function of the strut's slenderness ratio L/ρ listed in Tables 2 and 3. For failure of a strut with a high slenderness ratio, the Euler buckling load and stress (Ref. 19) are,

$$P_{euler} = -\pi^2 EI/L^2 \tag{4a}$$

$$\sigma_{euler} = -\pi^2 E/(L/\rho)^2. \tag{4b}$$

However, struts with lower slenderness ratios may buckle at a material strength-dependent load and stress defined as (Ref. 20),

$$P_{johns} = \sigma_{cy\text{-}m} A\{1 + [\sigma_{cy\text{-}m}(L/\rho)^2/(4\pi^2 E)]\} \tag{5a}$$

$$\sigma_{johns} = \sigma_{cy\text{-}m}\{1 - [\sigma_{cy\text{-}m}/(4\sigma_{euler})]\}. \tag{5b}$$

These buckling loads for the Strut *B* and *F* tubes are computed using the material and geometric properties from Table 1 and Eqns. 4 and 5, and are reported in Table 2.

The strut slenderness ratio at the transition point between these two buckling failure modes is computed by equating the stresses in Eqns. 4b and 5b, and then solving the resulting quadratic equation for the transition slenderness ratio $(L/\rho)_{trans}$, which is defined as,

$$(L/\rho)_{trans} = (-2\pi^2 E/\sigma_{cy\text{-}m}).^{1/2} \quad (6)$$

After substitution of the appropriate strut tube material properties into Eqn. 6, this transition slenderness ratio $(L/\rho)_{trans}$ is calculated as 49.2. Because Strut *F*'s computed slenderness ratio in Table 2 is greater than this transitional value, it will buckle as an Euler column at a load defined by Eqn. 4a. However, failure of Strut *B* is defined by Eqns. 5 because its slenderness ratio is less than the computed $(L/\rho)_{trans}$.

The effective bending stiffnesses for Struts *B* and *F* that include the Ti-6Al-4V end fittings and Inconel rod-end bearings are calculated from numerical analyses of the beams in three-point bending. These bending stiffness reductions of Struts *B* and *F* are calculated as 93.1 and 98.4 percent, respectively, of their baseline tube bending stiffnesses. These factors are applied to the baseline tube buckling loads in Table 2 to get the modified strut buckling loads listed in Table 3.

To also check against the possibility of material failure, the yield force P_{yield} for each strut is calculated using the mean compressive yield stress computed above,

$$P_{yield} = \sigma_{cy\text{-}m} A, \quad (7)$$

and reported in Table 2. Since Strut *A* is actually loaded in tension, Eqn. 7 is applied assuming that the tensile and compressive yield stress magnitudes are equal. The bolded and italicized critical failure loads P_{crit} = 30,867 lbf for Strut *A* in Table 2, and of −10,947 lbf and −4,242 lbf for Struts *B* and *F*, respectively, are listed in Table 3. The corresponding strut axial deformation Δ_{crit} is also computed in Table 3 as the ratio of the critical failure load P_{crit} and the effective strut axial stiffness K_{axial}.

To estimate the additional bending moment beyond buckling required to initiate yielding of a strut's outer wall at its midspan, the difference between the respective buckling axial stress and mean compressive yield stress is computed, and the yielding moment M_{yield} is calculated as,

$$M_{yield} = (P_{crit}/A - \sigma_{cy\text{-}m}) I/R. \quad (8)$$

The associated strut midspan lateral deflection Λ_{yield} is equal to the yield moment M_{yield} divided by the critical buckling load P_{crit}. The computed yield moments and midspan lateral deflections for Struts *B* and *F* are listed below in Table 4. To result in the permanent strut damage noted in the post-flight inspection, the bolded bending moment for Strut *F* in Table 4 must be assumed to have been exceeded, and therefore it represents a lower-bound estimate to the actual value.

For a sufficiently large bending moment, the material yields across the strut midspan and a plastic hinge (Ref. 21) will develop at point 4 in Fig. 12b. This failure represents a limiting value beyond which the strut would collapse and become a mechanism. The lateral deflection then increases without bound, as indicated by the horizontal dashed line in the figure. For a thin-walled tube, this plastic moment $M_{plastic}$ is derived as,

$$M_{plastic} = 4 (P_{crit}/A - \sigma_{cy\text{-}m}) R^2 T. \quad (9)$$

Although reported here, this particular failure mode is not considered credible to have occurred on STS-1, as the resulting strut deformation would have been quite large and readily observed

upon inspection. Total collapse of one or more of the tank support struts would also most likely have resulted in a catastrophic propellant tank failure.

Table 4. Strut bending failure

Strut	M_{yield}, lbf-in.	Λ_{yield}, in.	$M_{plastic}$, lbf-in.
A	—	—	—
B	758	0.069	1,127
F	***2,500***	0.589	3,388

XI. Tank Subsystem Failure Analysis

Equation of the oxidizer tank Strut *F*'s buckling load (−4,242 lbf from Table 3) to Eqn. 2f and solving for the unknown acceleration term returns a value of a_Z = +5.37 g. This is the quasi-static Z acceleration required to cause the fully loaded oxidizer tank (m_O = 1,537 lbm) to buckle the tank support Strut *F*. However, additional loading is still required to cause the bending, material yielding and plastic deformation noted on that strut.

The resulting axial strain energy U_{axial} for Strut *F* buckling is calculated as (Ref. 20),

$$U_{axial} = P_{crit}\Delta_{crit}/2 \tag{10}$$

or approximately 133 lbf-in. This first failure event is reported in Table 5 as value (1). This elastic failure is assumed to be followed by yielding of the strut wall at its midspan, resulting in the permanent damage found in the post-flight inspection. This yield failure results from a dynamic loading that caused a *minimum* bending moment M_{yield} of 2,500 lbf-in. reported above.

Table 5. Strut failure strain energy

Strut	U_{axial}, lbf-in.	U_{bend}, lbf-in.	U_{total}, lbf-in.
A	2,789	—	2,789
B	238 (2)	14	252 (3)
F	133 (1)	141	275 (4)

If the deflected shape of Strut *F* is assumed to be a half-sine wave (consistent with the assumed Euler buckling mode shape) with midspan lateral deflection Λ_{yield}, then the resulting bending strain energy U_{bend} is calculated as (Ref. 21),

$$U_{bend} = -\pi^2 \Lambda_{yield}^2 P_{euler}/(4L) \tag{11}$$

or 141 lbf-in., as listed in Table 5. This is 1.06 times the axial strain energy required for elastic buckling, and provides an estimate of the *minimum* dynamic amplification factor DAF that is required to cause the observed damage to Strut *F*,

$$DAF = (U_{axial} + U_{bend})/U_{axial}. \tag{12}$$

Substitution of the strain energies above results in a DAF = 2.06, with a minimum equivalent tank inertial loading required to damage Strut *F* to the level observed during STS-1 liftoff of at least (4,242 lbf x 2 x 0.9724 x 2.06), or 16,995 lbf (Eqn. 2f).

The axial strain energies required to fail the other loaded Struts *A* and *B* in tension and buckling, respectively, are also computed and listed in Table 5. The strain energy to buckle Strut *B*, denoted as item (2) in Table 5, is less than the total strain energy required to buckle and yield Strut *F*, denoted as item (4). The bending strain energy of 14 lbf-in. required to yield the Strut B mid-span wall is also calculated and reported in Table 5. This analysis therefore suggests that Strut *B* had buckled and yielded before Strut *F* failed in bending.

Substitution of the oxidizer tank mass and calculated $a_Z = +5.37\ g$ into Eqn. 2b results in a Strut *B* static force of −4,127 lbf. When multiplied by the 2.06 minimum DAF, the equivalent dynamic load in Strut *B* is −8,502 lbf. Since this calculated value is less than the force required to buckle Strut *B*, this result suggests that an upper bound for the actual DAF could actually be as large as (10,947 lbf/ 4,127 lbf), or 2.65. This higher DAF estimate of 2.65 may actually be better aligned with the physical evidence noted for Strut *F*, as the minimum DAF of 2.06 is only sufficient to initiate material yield at its midspan outer wall, and not to cause the more severe permanent deformation noted during post-flight inspection.

Examination of the strain energies listed in Table 5 suggests that the oxidizer tank support struts failed in the following order: Strut *F* buckled elastically first (1), followed by Strut *B* buckling (2) and then material yielding (3), and finally Strut *F* yielding in post-buckling bending (4). No empirical evidence of Strut *B* material failure, corresponding to value (3) in Table 5, was reported in Ref. 4. According to the results in Table 5, this yielding should have occurred well before the corresponding material failure of Strut *F* at value (4). One possible reason for this anomalous result may be that only static analyses were performed for this study. Because the force in Strut *F* cannot exceed the Euler buckling load, the static analysis does not account for any dynamic redistribution of the forces that should have taken place after that elastic buckling had occurred.

The discussion and analyses presented up to this point have been restricted to the oxidizer tank and its support struts, where the damage was observed. Another interesting possibility is whether Strut *F* on the less massive fuel tank had also failed under the same normal acceleration. Substitution of the full fuel tank mass ($m_F = 996$ lbm) and $a_Z = +5.37\ g$ above into Eqn. 2f results in a Strut *F* axial static force of −2,750 lbf, but does not exceed its Euler buckling load of −4,242 lbf. However, when that static force is multiplied by the minimum DAF of 2.06, the equivalent dynamic load in the fuel tank Strut *F does* exceed its buckling load, but is not large enough to also yield the strut outer wall. While no evidence of a failure of fuel tank Strut *F* was reported, this calculation suggests that that strut may have also buckled elastically at liftoff of STS-1. A corresponding failure of the fuel tank Strut *B* is not considered likely, as its static load under these conditions is only one-fourth of its buckling load.

XII. Concluding Remarks

As noted previously, the analyses performed in this study made certain simplifying assumptions on material behavior, strut geometry, and structural response. However, the actual material stress-strain response after yielding is most likely different from the idealized behavior that was assumed. Variations in the material yield stresses are also possible, and will affect the structure's actual behavior. Strut buckling loads are well known to be sensitive to boundary conditions and geometric imperfections, and are therefore almost certainly lower than the bounding values presented here. Their post-buckling responses are also likely to be affected by the initial imperfections.

Considering the caveats and assumptions made in this study, the results presented here should be considered a rough estimate for the actual structural response of the tank subsystem.

Further investigation using computational techniques such as finite element analyses that include dynamic effects and geometric and material nonlinearities could provide more realistic estimates for the time-varying strut loads, deflections, and resulting tank deformations.

In the end, NASA was very fortunate that none of the various incidents experienced on the Shuttle's inaugural flight cascaded into larger, systemic failures. However, before *Columbia* flew again in November 1981, great efforts were made across the agency to prevent a reoccurrence of the anomalies observed on STS-1. The effects of the ignition overpressure generated by the SRBs, which was the root cause of many of the problems noted, was greatly reduced for all subsequent flights by major modifications to the MLP sound suppression water system, and the strut loads were reassessed based on the actual flight data (Refs. 22, 23).

Composite reinforcements were bonded to the titanium tubes of Struts *B* and *F* supporting both FRCS module propellant tanks, following the same approach already baselined for the SSME thrust structure truss members in the orbiter aft fuselage. Unidirectional boron/epoxy plies, each 0.007 in. thick with a longitudinal modulus of 34 Mlbf/in^2, were bonded to the struts, greatly increasing their structural performance. The rod-end bearing diameters for the fuel tank support struts were also increased to match those on the oxidizer tank support struts. These mitigations were also applied to the other orbiters as they were built.

After *Columbia* landed safely at Edwards Air Force Base two days later, NASA JSC Director Christopher Kraft said, "*We just became infinitely smarter*." While inarguably true, were the risks taken worth the knowledge gained? The STS-1 crew, mission commander John Young and pilot Robert Crippen, were certainly fully aware and accepting of the risks inherent with the first flight of such a radically new launch system. The success of the mission is a fitting tribute to their bravery, and to the tremendous efforts of the government-industry team across the entire history of the Space Shuttle program.

This paper honors the memory of David R. Lowry, friend and colleague, who served the National Aeronautics and Space Administration as a technical leader at the Johnson Space Center until his untimely passing in 2016.

References

1. R. White, *Into The Black*: *The Extraordinary Untold Story of the First Flight of the Space Shuttle Columbia and the Astronauts Who Flew Her*, Atria Books, 2016.
2. D. R. Jenkins, *Space Shuttle, The History of the National Space Transportation System*, Specialty Press, Cape Canaveral, Florida, 2001.
3. R. D. Legler and F. V. Bennett, *Space Shuttle Missions Summary*, NASA/TM-2011-216142, September 2011.
4. Anon., *STS-1 Orbiter Final Mission Report*, NASA JSC-17378, August 1981.
5. R. S. Ryan, J. H. Jones, S. H. Guest, H. G. Struck, M. H. Rheinfurth, and V. S. Verderaime, *Propulsion System Ignition Overpressure for the Space Shuttle*, NASA TM-82458, December 1981.
6. S. Lai, *Development Of Space Shuttle Ignition Overpressure Environment And Correlation With Flight Data*, Shuttle Performance: Lessons Learned, NASA CP-2283, Part 1, J. P. Arrington and J. J. Jones, compilers, March 1983, pp. 481-488.
7. H. Ikawa and F. S. Laspesa, *Ignition/Duct Overpressure Induced by Space Shuttle Solid Rocket Motor Ignition*, AIAA J. Spacecraft and Rockets, Vol. 22, No. 4, July-August 1985, pp. 259-281.

8. K. Bernstein, G. James, A. Mackey, C. T. Modlin, N. C. Murphy, and S. Brolliar; *Shuttle Program Loads Integration: Going From Concept to Operations and Staying Successful*, AIAA Space 2011 Conference, Long Beach, California, September 2011, AIAA 2011-7123.
9. D. R. Blevins and C. W. Hohmann, *Description of the Space Shuttle Reaction Control System*, AIAA/SAE 11th Propulsion Conference, Anaheim, California, September 1975, AIAA 75-1299.
10. P. R. Edwards, F. C. Svenson, and F. O. Chandler, *The Development and Testing of the Space Shuttle Reaction Control System*, ASME Winter Annual Meeting, San Francisco, California, December 1978, Paper No. 78-WA/Aero-20.
11. Anon., *Shuttle Operational Data Book (Volume 2)*, NASA JSC-08934, September 1995. http://www.spaceflight.nasa.gov/shuttle/reference/sodb/213a.pdf
12. R. Peterson and P. Uney, *Development and Qualification of the Space Shuttle Orbiter Reaction Control System Propellant Tank*, AIAA/SAE 14th Propulsion Conference, Las Vegas, Nevada, July 1978, AIAA 78-1026.
13. R. A. Boudreaux, *Orbiter OMS and RCS Technology*, Satellite Services Workshop, Vol. 1, pp. 406-430. NASA TM-84873, June 1982.
14. Anon., *OV-102 Stress Analysis, STS-1 Loads Assessment, Forward Fuselage − Upper*, Rockwell International, SOD 80-0085, Volume 4, Contract NAS 9-14000, IRD NO. SE-767T2, WBS 1.3.1, December 1980.
15. C. T. Modlin, Senior Engineer, NASA Johnson Space Center (retired), personal communications, May-July 2019.
16. Anon., *Space Shuttle Orbiter Reaction Control Subsystem*, Rockwell International, November 1989.
17. S. P. Timoshenko and D. H. Young, *Theory of Structures, 2nd Edition*, McGraw-Hill, 1965.
18. Anon., *Structural Design Criteria Applicable To A Space Shuttle*, NASA SP-8057, revised March 1972.
19. S. P. Timoshenko and J. M. Gere, *Theory of Elastic Stability, 2nd Edition*, McGraw-Hill, 1961.
20. F. P. Beer and E. R. Johnston, *Mechanics of Materials*, McGraw-Hill, 1981.
21. I. A. Karnovsky and O. Lebed, *Advanced Methods of Structural Analysis*, Springer, 2010.
22. R. S. Ryan, *Problems Experienced and Envisioned for Dynamical Physical Systems*, NASA TP-2508, August 1985.
23. J. C. Blair, R. S. Ryan, and L. A. Schutzenhofer, *Lessons Learned in Engineering*, NASA/CR-2011-216468, June 2011.
24. Anon., *Metallic Materials And Elements For Aerospace Vehicle Structures*, MIL-HDBK-5H, December 1998.
25. D. M. Lane, *Online Statistics Education: A Multimedia Course of Study*, http://onlinestatbook.com/

Appendix A. Solution of Equilibrium Equations

If the axial load in each strut is initially assumed to be tensile, the six, 3-dimensional equilibrium equations for the simplified tank subsystem model in Fig. 10 are

$$\Sigma F_X = 0: \ -\mathrm{P}_A + ex\,\mathrm{P}_E - fx\,\mathrm{P}_F = 0 \tag{A1}$$

$$\Sigma F_Y = 0: \ cy\,\mathrm{P}_C + dy\,\mathrm{P}_D + ey\,\mathrm{P}_E = 0 \tag{A2}$$

$$\Sigma F_Z = 0: \ \mathrm{P}_B - cz\,\mathrm{P}_C + dz\,\mathrm{P}_D - ez\,\mathrm{P}_E + fz\,\mathrm{P}_F + m\,\mathrm{a}_Z = 0 \tag{A3}$$

$$\Sigma M_X = 0: \ -cy\,\mathrm{P}_C\mathrm{r} + dy\,\mathrm{P}_D\mathrm{r} = 0 \tag{A4}$$

$$\Sigma M_Y = 0: \ \mathrm{P}_B\mathrm{R} - cz\,\mathrm{P}_C\mathrm{R} + dz\,\mathrm{P}_D\mathrm{R} + ez\,\mathrm{P}_E\mathrm{R} - fz\,\mathrm{P}_F\mathrm{R} = 0 \tag{A5}$$

$$\Sigma M_Z = 0: \ -cy\,\mathrm{P}_C\mathrm{R} - dy\,\mathrm{P}_D\mathrm{R} + ey\,\mathrm{P}_E\mathrm{R} = 0. \tag{A6}$$

The moments in Eqns. A4 to A6 are calculated with respect to the tank center of mass. The italicized terms (*e.g.*, *ex* for Strut *E* and *fx* for Strut *F*, in Eqn. A1) are the struts' direction cosines shown in Fig. 10. After factoring the forward fitting radius r out of Eqn. A4, and the tank radius R out of Eqns. A5 and A6, these equations become

$$cy\,\mathrm{P}_C - dy\,\mathrm{P}_D = 0 \tag{A4a}$$

$$\mathrm{P}_B - cz\,\mathrm{P}_C + dz\,\mathrm{P}_D + ez\,\mathrm{P}_E - fz\,\mathrm{P}_F = 0 \tag{A5a}$$

$$cy\,\mathrm{P}_C + dy\,\mathrm{P}_D - ey\,\mathrm{P}_E = 0. \tag{A6a}$$

The magnitudes of the direction cosines for Struts *C* and *D* are equal in the Y and Z directions, so $cy = dy$ and $cz = dz$, respectively. Solution of Eqn. A4a gives $\mathrm{P}_C = \mathrm{P}_D$, and elimination of those terms from Eqn. A5a results in

$$\mathrm{P}_B + ez\,\mathrm{P}_E - fz\,\mathrm{P}_F = 0. \tag{A5b}$$

Addition of a simplified Eqn. A3 and Eqn. A5b gives $\mathbf{P_B = -m\,a_Z/2}$, where the negative sign indicates a compressive load. Subtraction of Eqn. A2 from Eqn. A6a gives $2\,ey\,\mathrm{P}_E = 0$, which can only be true if $\mathbf{P_E = 0}$, given that $ey \neq 0$. Substituting derived values of P_B and P_E into Eqn. A5b results in $\mathbf{P_F = -m\,a_Z/(2fz)}$. Substituting values of P_E and P_F into Eqn. A1 then gives $\mathbf{P_A = +fx\,m\,a_Z/(2fz)}$. Using $\mathrm{P}_C = \mathrm{P}_D$ and $\mathrm{P}_E = 0$, solution of Eqn. A2 gives $\mathbf{P_C = P_D = 0}$.

To check the validity of this solution, the bolded strut forces above are substituted into the equilibrium equations. Substituting the non-zero forces into Eqns. A1, A3, and A5b gives

$$-[+fx\,m\,\mathrm{a}_Z/(2fz)] - fx\,[-m\,\mathrm{a}_Z/(2fz)] \Rightarrow 0 \tag{A1a}$$

$$-m\,\mathrm{a}_Z/2 + fz\,[-m\,\mathrm{a}_Z/(2fz)] + m\,\mathrm{a}_Z \Rightarrow 0 \tag{A3a}$$

$$-m\,\mathrm{a}_Z/2 - fz\,[-m\,\mathrm{a}_Z/(2fz)] \Rightarrow 0. \tag{A5c}$$

These equalities confirm that the set of forces summarized in Eqns. 2a through 2f in Section VIII provides a valid solution to the equilibrium equations. This problem also simplifies to an equilibrium analysis in the X-Z plane.

Appendix B. Calculation of Mean Stresses

Reported design allowable stress values for titanium Ti-6Al-4V alloy are used to estimate the mean compressive yield stress $\sigma_{cy\text{-}m}$ for the Ti-3Al-2.5V material used to build the struts. The A-basis (99 percent probability, 95 percent confidence) allowable tensile ultimate stress for Ti-6Al-4V bar (Ref. 14) $\sigma_{tu\text{-}A} = 130$ klbf/in^2, with a B-basis (90 percent probability, 95 percent confidence) allowable stress $\sigma_{tu\text{-}B} = 138$ klbf/in^2 (Ref. 24). This datapoint is plotted in Fig. B1 as the white circle. From the same references, the A- and B-basis allowable tensile yield stresses $\sigma_{ty} = 120$ klbf/in^2 and 128 klbf/in^2, respectively, are plotted as the white square in Fig. B1.

Analysis of a standard normal distribution with mean M = 0 and standard deviation S = 1 (Ref. 25) shows that the 99 percent probability interval corresponding to the A-basis allowable occurs at a standard deviation of −2.325. A similar analysis for the B-basis allowable has a 90 percent probability interval occurring at a standard deviation of −1.282. Substitution of the Ti-6Al-4V allowable tensile ultimate stresses σ_{tu} into equations for the unknown mean allowable stress M and corresponding standard deviation S gives

$$M - 2.325\,S = 130 \text{ klbf/in}^2 \text{ (A-basis)} \quad \text{(B1)}$$

$$M - 1.282\,S = 138 \text{ klbf/in}^2 \text{ (B-basis).} \quad \text{(B2)}$$

Simultaneous solution of these equations for the mean tensile ultimate stress gives $\sigma_{tu\text{-}m}$, = 147.83 klbf/in^2, and a standard deviation S = 7.67 klbf/in^2. A similar solution for the mean tensile yield stress gives $\sigma_{ty\text{-}m} = 137.83$ klbf/in^2, with the same standard deviation S = 7.67 klbf/in^2. These mean values are shown in Fig. B1 as the gray circle and square, respectively. The linear relationship between the A-basis and B-basis tensile stresses is plotted as the solid line in Fig. B1, and the corresponding relationship between the A-basis and mean tensile stresses is plotted as the dashed line. The Ti-3Al-2.5V material used for the support struts has an A-basis design allowable compressive yield stress $\sigma_{cy\text{-}A} = -108$ klbf/in^2 (Ref. 14). The magnitude of that stress is assumed to correspond to a mean compressive yield stress $\sigma_{cy\text{-}m} = -125.83$ klbf/in^2, whose magnitude is plotted as the black diamond in Fig. B1.

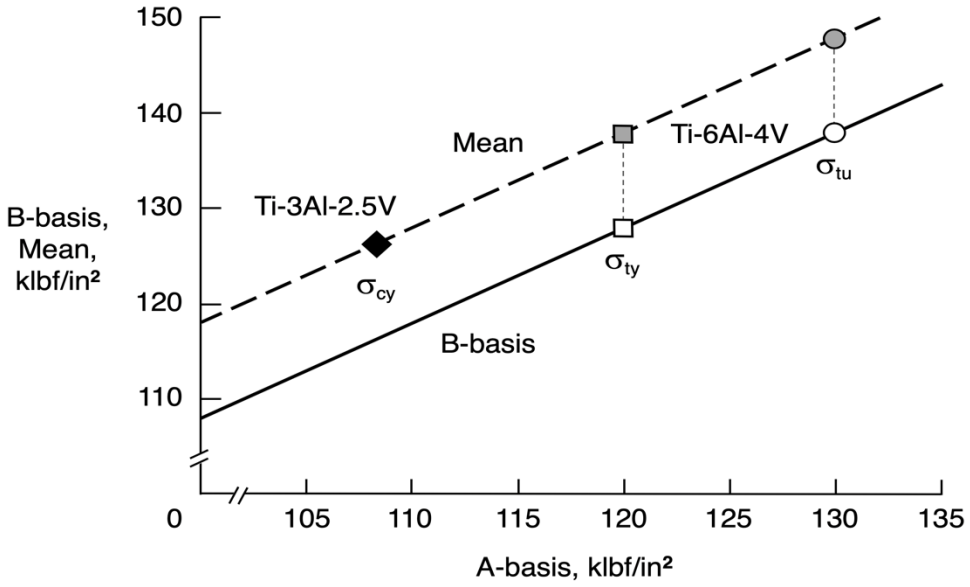

Figure B1. Titanium stress values